https://doi.org/10.5194/essd-2025-609
Preprint. Discussion started: 3 March 2026

Open Access Earth System Science Data Discussions

Atmospheric and cryospheric observations at the high-altitude Zarafshon River Basin and the Hydrographic Party Glacier (GGP), Tajikistan, 2018-2025

Jonas Svensson[1], Ramazon Rakhmonov[2], Kamoliddin Nazirzoda[2], Abdusamad Hojiev[2], Tamlikho Jurabekov[2], Amirsho Hiyoev[2], Davlatjon Rahimzoda[2], Hizbullo Kholzoda[2], Muzaffar Shodmonov[2], David Brus[1], Viet Le[1], Krista Luoma[1], Adriano Lemos[1], Germán Perez Fogwill[1], Meri M. Ruppel[1], Outi Meinander[1], Johan Ström[3], Eija Asmi[1], Antti Hyvärinen[1]

[1]Finnish Meteorological Institute, Erik Palménin aukio 1, FI-00506, Helsinki, Finland

[2]Agency for Hydrometeorology, Committee of Environmental Protection under the Government of the Republic of Tajikistan, Street B, Gafurov 373, Dushanbe, Tajikistan

[3]Department of Environmental Science, Stockholm University, 106 91 Stockholm, Sweden

Correspondence to: Jonas Svensson (jonas.svensson@fmi.fi)

Abstract. Central Asia is a region with high-altitude mountains, hosting numerous glaciers and widespread seasonal snow cover, both of which have an integral role in the regional hydrological cycle. Despite their importance, observations of cryospheric and atmospheric variables are scarce in this area but are essential to assess the temporal and spatial changes induced by climate change. To address this gap, we present a diverse data set of cryospheric and atmospheric variables from the Zarafshon River Basin and the Hydrographic Party Glacier (GGP) in Tajikistan, spanning the time frame of 2018–2025. The data includes glacier terminus position and snow conditions, glacier ablation, high resolution aerial photography, meteorological variables, surface reflectance combined with snow chemistry, and atmospheric aerosol concentrations. These observations provide a valuable basis for research on glacier dynamics, snow processes, and atmosphere-cryosphere interactions in a region where monitoring has been sparse. The data are available at the Finnish Meteorological Institute data repository METIS: https://doi.org/10.57707/fmi-b2share.t4vwg-gf542 (Svensson et al., 2026).

https://doi.org/10.5194/essd-2025-609
Preprint. Discussion started: 3 March 2026

1 Introduction

Central Asia (CA) is an area characterized by mountainous terrain, forming the northwestern periphery of high-mountain Asia (HMA). The major mountain ranges of Tian Shan and Pamir host numerous glaciers and have extensive seasonal snow cover, both of which have an instrumental role in the regional hydrological cycle (e.g., Chen et al., 2016). The runoff from snow- and glacier melt are critical for downstream rivers, with the glacier melt being particularly important during periods of draught, since it continuously produces runoff unlike seasonally fluctuating snow melt (Pohl et al., 2017). While the snow and ice melt input to river discharge is expected to increase in the future, the runoff is projected to diminish in the long-term, reinforcing the regional water stress levels (Pritchard, 2019). Our understanding of the changing regional CA cryosphere, both spatial and temporally, is currently limited due to a lack of observations. The absence of observations hampers deduction of the driving meteorological and morphological variables on glacier changes for the Tian Shan and Pamir regions (Barandun and Pohl, 2023).

The overall net changes on cryospheric variables are primarily the result of different atmospheric processes. For instance, precipitation can exert a strong control on glacier and snow accumulation. In CA precipitation varies strongly spatially, while the general pattern reflects higher precipitation in the west and more arid conditions towards the east (e.g., Aizen et al., 1995). Precipitation, and snowfall specifically, is challenging to measure, with mountain precipitation being systematically underestimated on the order of 50–100% (e.g., Beck et al., 2020; Pritchard, 2021). In addition, nearly all long-term observations of precipitation are typically from weather stations that are below 3 000 m. Consequently, precipitation amounts are poorly quantified throughout HMA (Chen et al., 2016). The ablation of glacier and snow mass is driven by atmospheric warming, which in HMA proceeds at a rate that is twice as fast as the global average (e.g., You et al., 2021). Another important factor that affects ablation is the absorption of solar radiation, which is mostly dictated by the surface albedo (Marks and Dozier, 1992). For HMA, the albedo of glaciers has declined in the last decades, and this decline is an important driver for glacier recession, especially in the Tibetan Plateau and its surroundings (Zhang et al., 2021).

During the Soviet era, monitoring environmental variables in CA was relatively extensive (e.g., Aizen et al., 1995), but most observations came to an abrupt halt following the collapse of Soviet Union in the mid 1990's. Since then, great efforts have been made during the 2010's to re-establish observations in the area. Glacier monitoring has been restarted on some glaciers in Uzbekistan and Kyrgyzstan (Hoelzle et al., 2017), as well as some additional glacier observations and other cryospheric variables outlined in Barandun et al. (2020). Hydrometeorological stations (n = 18) that are remotely operated in CA are also nowadays present and are further outlined in Zech et al. (2021). Nonetheless, current cryospheric and atmospheric measurements remain acutely scarce throughout the CA region.

To meet the observational gap, the Finnish Meteorological Institute (FMI) and the Agency for Hydrometeorology of Tajikistan (Hydromet) began a joint effort to reinstate observations in Tajikistan at the Hydrographic Party Glacier, hereafter referred to as GGP, located in the Zarafshon River Basin. This selected site was originally visited for measurements for the first time in 1968, and some key observations from those years indicated that GGP was 1.4 km in length, in a steady state, and had a volume of 0.0270 km^3 (Vladimirova et al., 1976). In the subsequent years of visits (between 1972 and 1974) stationary observations were carried out on the glacier, in a program that included glaciological, snow measurement, meteorological, hydrological, and actinometric observations. In 2018 the Hydromet together with FMI began annual scientific research and field work at GGP glacier (Figs. 1a–b). Being a small temperate cirque-valley glacier with typically winter accumulation, GGP has a northward facing orientation and is situated at the elevation range 3600–3800 m a.s.l. The closest major city is the capital of Tajikistan, Dushanbe, at about an aerial distance of 60 km south-east. Thus, the investigation area is readily accessible. Vehicle transportation from Dushanbe via the Iskanderkul lake to a nearby drop off point is available within a few hours, after which an expedition base camp can be reached within a day on foot (~10 km). Here, in this paper, we focus on describing the more recent data that has been collected cooperatively based on six field expeditions that took place in August or September of 2018 2019, 2021, 2023, 2024, and 2025. In addition, some standalone instruments (in particular, the automatic weather sensors) measured continuously outside of the expedition periods. In this paper we first present our used methodologies (Sect. 2), then describe the existing observation data sets and present key results (Sect. 3), and lastly summarize our work.

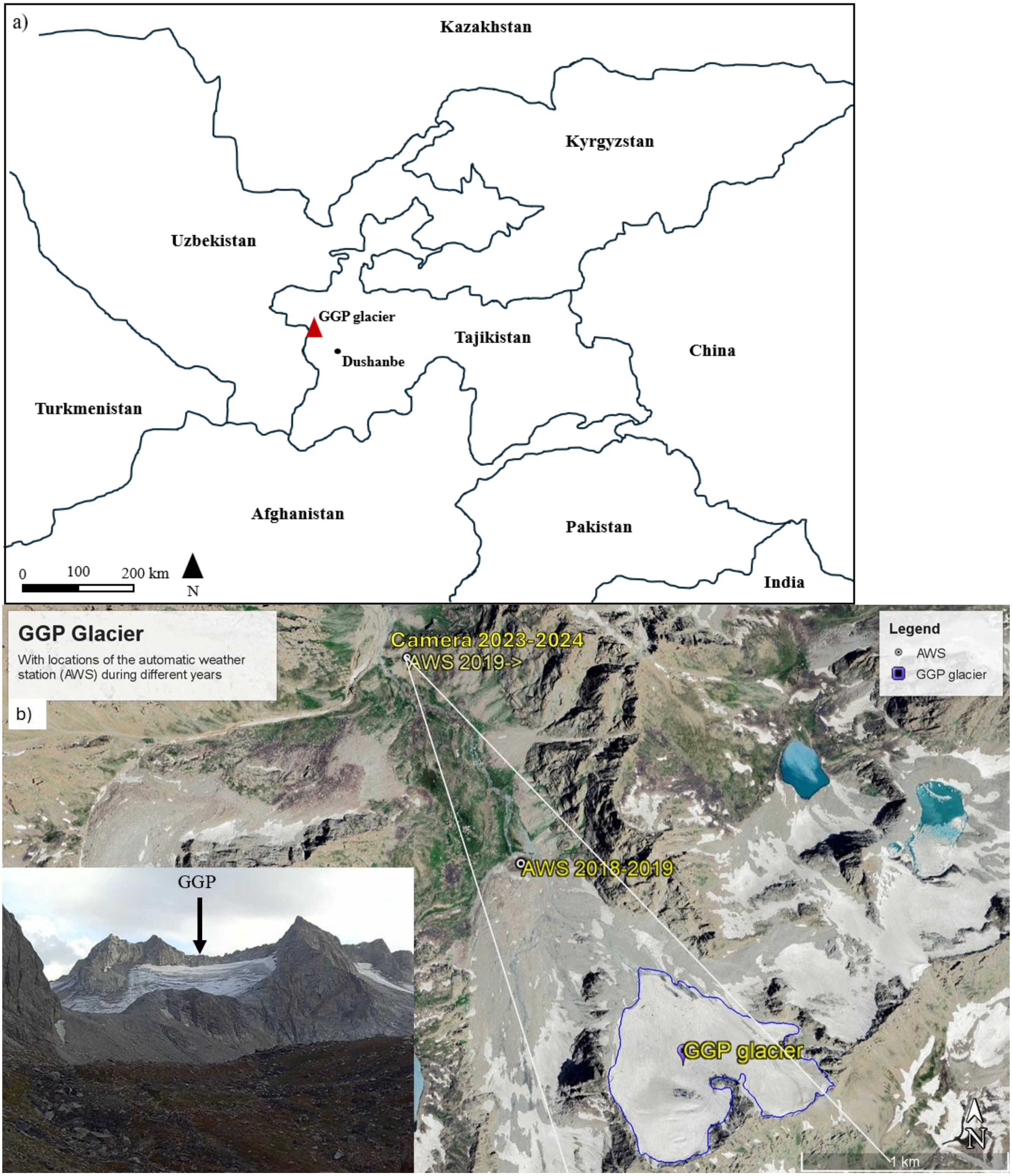

Figure 1. a) Map of Central Asia and Tajikistan with the location of GGP indicated by red triangle. b) Satellite imagery of the study

area with an inserted image of GGP (in bottom left) as seen from the weather station camera 2023-09-04. AWS stands for automatic weather station. Field of view of the camera installed in 2023 is indicated with white lines. Image source Google Maps (© Google 2025).

2 Material and methodologies

2.1 Remote sensing of GGP terminus

The glacier extent and terminus shift of GGP has been monitored by remote sensing since 1989, by multispectral Landsat-5, Landsat-7 and Landsat-8 missions provided by the National Aeronautics and Space Administration and the United States Geological Survey, and more recently, by the systematic Sentinel-2 (S2) satellite constellation provided and launched by the European Space Agency (optical imaging component of the European Commission's Copernicus Earth Observation satellite program). The operational period of the satellites Landsat-5, -7, and -8, are between March 1984 – January 2013, April 1999 – April 2022, and February 2013 – current, respectively. Currently, the S2 constellation consists of three satellites. The first, Sentinel-2a, was launched in June 2015, followed by Sentinel-2b in March 2017, and Sentinel-2c in September 2024. The ice front variation of GGP was determined based on methodology in Moon and Joughin (2008). First, an opened box was delineated, covering the glacier and taking the base of the opened box as a reference line (Fig. S1). Then, each ice front is manually digitized from the satellite images. The mean retreat or advance of the glacier is determined by the area change divided by the width of the box. This methodology better assesses the ice front variation, accounting for uneven changes at the ice front (Moon and Joughin, 2008).

2.2 Aerial photography of GGP

During the expeditions in 2018, 2019, 2023, and 2024, aerial photography utilizing semi-professional grade quadcopters DJI models Phantom 4 pro and Phantom 4 pro V2 were used to collect high resolution images. The Phantom 4 Pro (including upgraded V2) has all-up weight of 1375 g and is equipped with a 1-inch sensor which has resolution of 20 million effective pixels (5472 × 3648 pixels). Using rechargeable 5870 mAh Lithium polymer (LiPo) battery, the drone is capable of a max manufacturer stated flight time of 30 min and a signal transmission distance of 7 km. In practice, the drone was able to fly for about 20 min at about 4 km altitude with occasional transmission problems. One drone was lost throughout the expedition years due to unresolved transmission issues.

To process the collected images the stand-alone version of Pix4Dmapper software version 4.9.0 was used utilizing the hardware: CPU: Intel(R) Core (TM) i7-8750H CPU at 2.20 GHz; RAM: 64 GB; GPU: Intel(R) UHD Graphics 630, NVIDIA Quadro P1000; and operating system: Windows 10 Pro, 64-bit. The drones' cameras were calibrated automatically as a part of the internal Pix4D mapper software structure from motion (SfM) process. During our expeditions' aerial photography missions, no ground control points (GCPs) were used in 2018 and 2019 due to various logistical and weather issues. To mitigate this incompleteness, Google Earth was used to create GCPs artificially by using significant natural check points such as large boulders or part of rock spread around the glacier. During 2023 and 2024 the drilled ablation stakes positions were marked with red crosses of about 2 m arm length, but not all of them were found on acquired images. Our main interest was to map the glacier terminus, and to generate the digital surface models (DSM) and orthomosaic overlays of GeoTIFF and Google Maps tiles. The WGS84/UTM zone 42N (EGM 96 Geoid) coordinate system was used.

The following processing settings were used: key points image scale: full; image scale: 1; calibration: automatic; calibration method: standard. point cloud densification image scale: multiscale, 1⁄2 (half image size); point density: optimal; minimum number of matches: three; matching image pairs: aerial grid or corridor; targeted number of key points: automatic; rematch: automatic; 3D textured mesh: medium resolution, use color balancing for textures.

2.3 GPS survey of GGP terminus

The glacier terminus location was mapped during the expeditions in 2018, 2023, 2024, and 2025 with a GPS (Garmin SPS 72H and Garmin inReach Mini2) device, through traversing the terminus and recording the borders, or by taking several individual coordinate readings along the terminus transect. The approximate accuracy of the measurement is within 5 to 10 m under normal conditions

2.4 Time-lapse photography of GGP

An automatic camera (Hunter Basic Trail Camera) was installed during the 2023 expedition in conjunction with the automatic weather station (AWS) to record the prevailing environmental conditions at the AWS site and at GGP. The camera operates with 12 AA-batteries and automatically takes one daily image (at ~0900 UTC+5), which are stored on an internal SD-card.

2.5 Ablation stake survey

Glacier ablation was measured with the conventional glaciological method (e.g., Cogley et al., 2011), with stakes being drilled into the ice throughout the glacier ablation zone, which are traditionally transformed into ice ablation by multiplying the height change by an assumed ice density of 900 kg m^{-3} (Cogley et al., 2011). Stakes with a height of 4 m (consisting of two 2 m individual stakes connected) were inserted into holes that were drilled with a handheld electronic drill connected to an ice auger with connectable auger flights (Kovacs Ice Drilling Equipment). The position parameters of the stakes were recorded with a GPS. During the following years' expeditions, the stakes were measured. In case of broken stakes, replacement stakes were installed in the ice.

2.6 Meteorological measurements

An AWS (Vaisala MAWS 201) was installed in 2018 adjacent to the glacier front (although this location had to be shifted, see data specifics below in Sect. 3.6) for long-term continuous observations of the meteorological parameters. The AWS measures temperature (*T*), relative humidity (*RH*), precipitation (*P*), pressure (*p*), wind speed (*WS*), wind direction (*WD*), solar global irradiance (*GI*), and snow depth (*SD*). The AWS operates with a 37 W solar panel and three 7 Ah, 12 V batteries. The measured parameters together with sensors used are described in Table 1, while the AWS is visualized in Fig. 2. The precipitation gauge is not heated; thus, the precipitation record is limited to recording liquid. It may, therefore, possibly include melt from accumulated snow also. All parameters are measured with a 10 s time resolution and can be transmitted remotely via Iridium modem.

Table 1. Sensor specifications installed on the automatic weather station.

Parameter	Sensor	Range/resolution	Accuracy
Temperature (T)	Vaisala HMP155	-40 to +60 °C	± $(0.226–0.0028 \times T)$ °C
Relative humidity (RH)		0–100%	±1%
Rain/Precipitation (P)	Vaisala QMR101	0.2 mm	±2%
Pressure (p)	Vaisala BARO-1	500–1100 hPa	±0.05 hPa
Wind speed and -direction (WS and WD)	Vaisala WMS302M	0.5–60 m s^{-1}	±0.3 m s^{-1}
Solar global irradiance (GI)	Kipp & Zonen CMP3 pyranometer	300–2800 nm	±15 W m^{-2}
Snow depth (SD)	Campbell SR50AH	0.5–10 m	± 1 cm

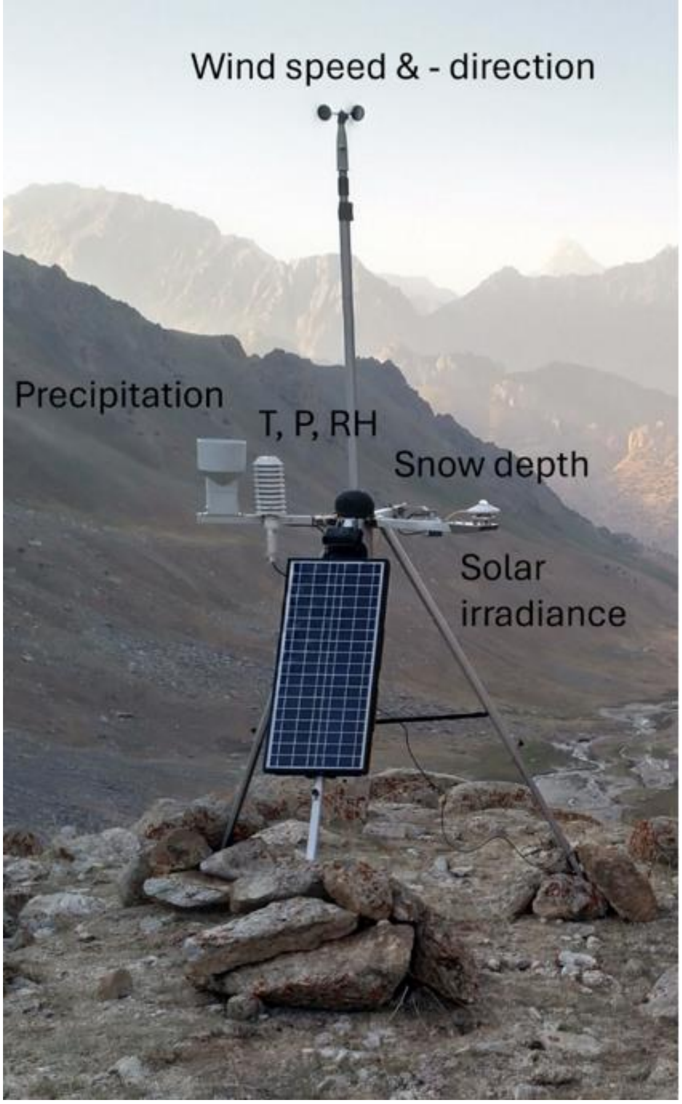

Figure 2. Photograph of AWS with the different sensors indicated (T = temperature, P = pressure, RH = relative humidity).

2.7 Glacier snow chemistry

To study the snow impurities at GGP different types of snow samples were collected in the expeditions of 2018 and 2019 via surface snow collection and excavation of snow pits. This sampling was conducted in connection with surface reflectance measurements (Sec. 2.8). The snow pit samples were sampled in height intervals from 3 to 10 cm and were melted and filtered onto 47 mm micro-quartz fiber filters in the field following the principles of Svensson et al. (2018). In the laboratory a filter punch was analyzed for carbonaceous particles, i.e. elemental- and organic carbon content, with a thermal-optical analyzer (Sunset Laboratory Inc., Birch and Cary, 1996) utilizing the EUSAAR-2 protocol (Cavalli et al., 2010). A second filter punch from selected substrates was further analyzed for trace metals (Aluminum, Arsenic, Cadmium, Cobalt., Chromium, Copper, Iron, Manganese, Nickel, Lead, Vanadium, Zinc) with an inductively coupled plasma mass spectroscopy (ICP-MS, Thermo iCAP Q). Prior to analysis, this filter punch was digested microwave-assisted (utilizing Milestone Ultrawave 3) in acid solution (Nitric acid + Hydrogen peroxide) according to the standard SFS-EN 14902. The combustion temperature of 250 °C deviates from the standard's 220 °C but was used in order to maximize the yield of less soluble analytes (Aluminum, Chromium, Vanadium). Internal standards (Scandium, Gallium, Rhodium, Iridium) were added to the samples before combustion. Surface snow samples were collected in 20 mL glass vials and transported back to Helsinki in a melted state but light-protected state to the laboratory in Finland .. The surface snow samples were filtered (Accrodisc pore size 0.45 µm) and analyzed for inorganic ions (Sodium, Ammonium, Potassium, Magnesium, Calcium, Chloride, Nitrate, Sulfate) with two ion chromatographs (Waters).

2.8 Glacier surface reflectance

The prevailing surface reflectance at the glacier, in connection with snow sampling, was determined with a handheld spectroradiometer, ASD FieldSpec HandHeld 2 (Malvern Panalytical Ltd; spectral range 325–1075 nm) during the 2019 and 2023 campaigns. Different areas from the glacier surface that appeared to be representative of the specific years' expedition were selected for measurements. Time periods of stable lighting conditions, i.e., avoiding changing cloudiness or partially cloudy circumstances, were utilized for these measurements. To minimize the impact of solar zenith angle of the reflectance, the measurements at different locations were performed at similar times of the day. The measurements were conducted by first taking a white reference measurement (Spectralon Labsphere Inc.), followed by measurements of the glacier surface, and finally followed by another white reference measurement. This allowed minimizing the effects of instrument response to changes of the field brightening conditions.

2.9 Atmospheric aerosol

During our field expeditions to GGP, measurements of atmospheric aerosols were performed with portable instrumentation at a height of 1.5 m above the ground surface. These included aerosol absorption (which can be used to infer black carbon concentrations), particle number concentration, and particle size distribution at the size range from 0.3 µm to 10 µm. The absorption was measured with a Microaethalometer AE51 (AethLabs) in the 2018 and 2019 campaigns, and with the Microaethalometer MA350 (AethLabs) in the 2021 and 2023 campaigns. Particle total number concentration >10 nm was measured with a condensation particle counter (TSI model 3007) and the particle size distribution with an optical particle counter, both measured during the 2018 campaign only.

185 ## 3. Description of datasets and key results

Data availability from the different expeditions, as well as the continuous measurements are presented in Table 2, followed by the subsequent subchapters further describing each dataset in more detail. The spatial distribution of the different point scale measurements from the glacier are further highlighted in Fig. 3.

190 **Table 2. Observation parameters and data availability of this study. Abbreviations for different meteorological parameters are given in Table 1.**

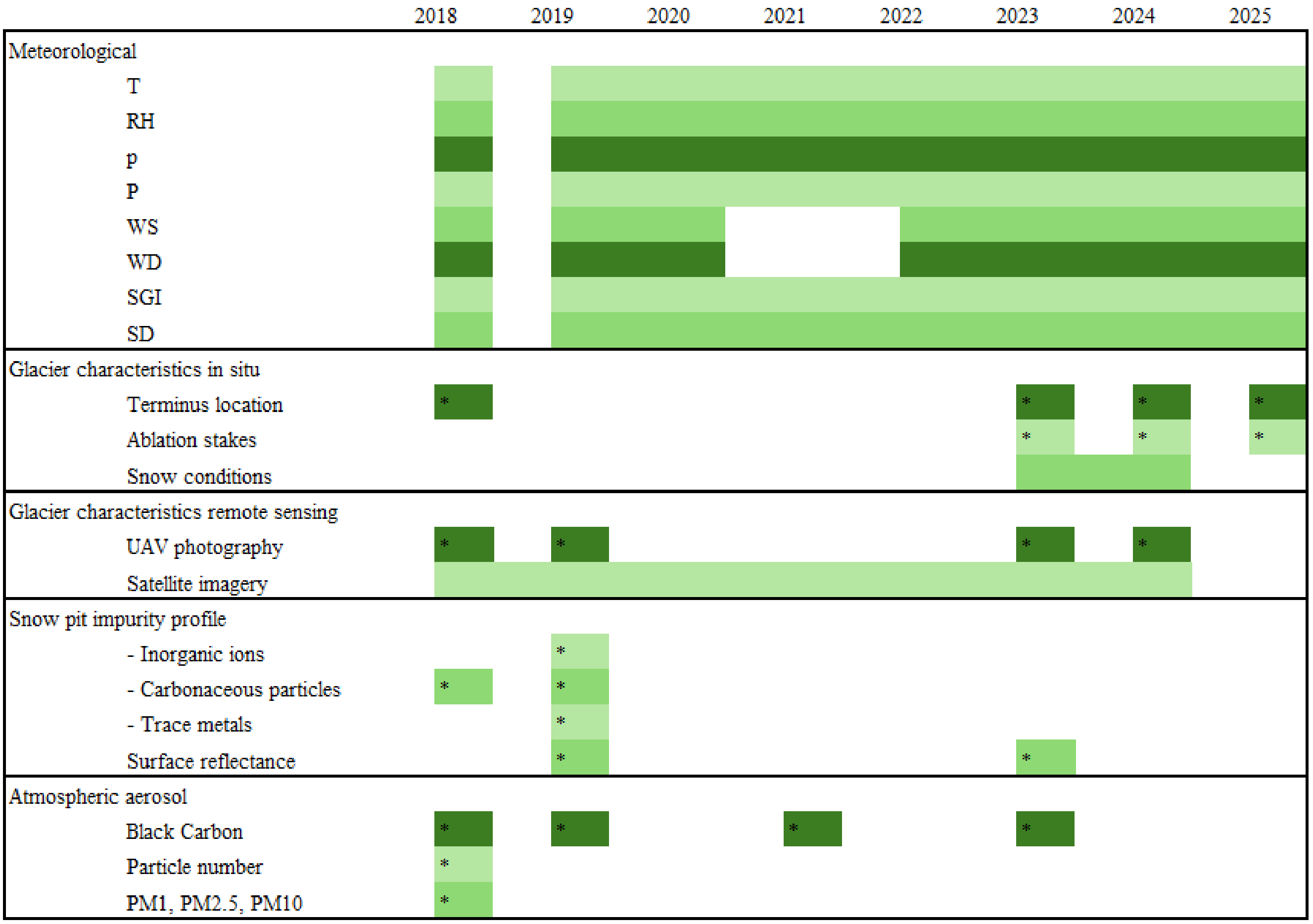

	2018	2019	2020	2021	2022	2023	2024	2025
Meteorological								
T	🟩	🟩	🟩	🟩	🟩	🟩	🟩	🟩
RH	🟩	🟩	🟩	🟩	🟩	🟩	🟩	🟩
p	🟩	🟩	🟩	🟩	🟩	🟩	🟩	🟩
P	🟩	🟩	🟩	🟩	🟩	🟩	🟩	🟩
WS	🟩	🟩	🟩		🟩	🟩	🟩	🟩
WD	🟩	🟩	🟩		🟩	🟩	🟩	🟩
SGI	🟩	🟩	🟩	🟩	🟩	🟩	🟩	🟩
SD	🟩	🟩	🟩	🟩	🟩	🟩	🟩	🟩
Glacier characteristics in situ								
Terminus location	*					*	*	*
Ablation stakes						*	*	*
Snow conditions						🟩	🟩	
Glacier characteristics remote sensing								
UAV photography	*	*				*	*	
Satellite imagery	🟩	🟩	🟩	🟩	🟩	🟩	🟩	
Snow pit impurity profile								
- Inorganic ions		*						
- Carbonaceous particles	*	*						
- Trace metals		*						
Surface reflectance		*				*		
Atmospheric aerosol								
Black Carbon	*	*		*		*		
Particle number	*							
PM1, PM2.5, PM10	*							

*) Measurements during expeditions: 2018.9.18-22, 2019.8.31-3.9, 2021.9.17-21, 2023.9.3-7, 2024-9.16-18, 2025.8.27-30

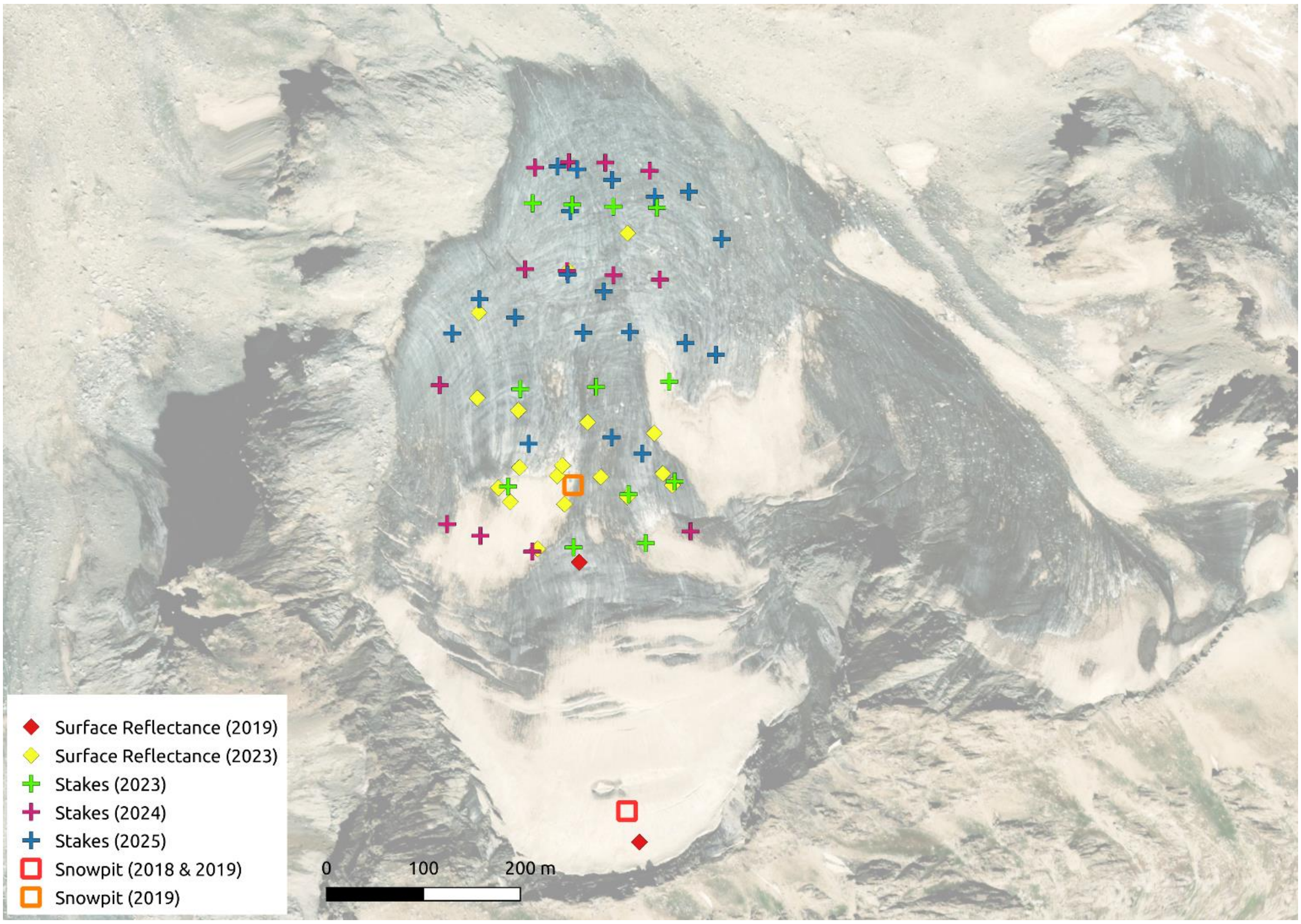

Figure 3. Location of surface reflectance, ablation stakes, and snow pits point measurements conducted at GGP. Image source Bing Maps (© Microsoft) and imagery data © 2025 Maxar.

3.1 Remote sensing of GGP terminus

The 13-cloud free images utilized to delineate the glacier frontal extent, from Landsat-5, Landsat-7, Landsat-8, and Sentinel-2 satellites, are listed in Table 3. Landsat-5 carried the Thematic Mapper (TM), collecting data across seven bands, including visible, near-infrared, mid-infrared, and thermal infrared spectrum. Landsat-7 used the Enhanced Thematic Mapper Plus (ETM+), including a high-resolution panchromatic band, improved radiometric calibration, and a thermal infrared channel. Landsat-8 further advanced the series with two instruments, the Operational Land Imager (OLI) and the Thermal Infrared Sensor (TIRS), with spatial resolutions of 30 m for most bands, 100 m for thermal, and 15 m for panchromatic imagery. Moreover, each Sentinel-2 satellite carries the Multi-Spectral Instrument (MSI), acquiring images within 13 different spectral bands at spatial resolutions ranging from 10 m to 60 m, covering the visible, near-infrared, and shortwave infrared regions.

Table 3. Satellite imagery used to delineate ice front locations and the glacier extent.

Date (yyyy-mm-dd)	Mission	Product ID
1989-09-24	Landsat-5	LT05_L1TP_154033_19890924_20200916_02_T1
2000-08-29	Landsat-7	LE07_L1TP_154033_20000829_20200918_02_T1
2010-09-10	Landsat-7	LE07_L1TP_154033_20100910_20200911_02_T1
2012-09-15	Landsat-7	LE07_L1TP_154033_20120915_20200908_02_T1
2014-09-05	Landsat-7	LE07_L1TP_154033_20140905_20200906_02_T1
2016-09-10	Landsat-7	LE07_L1TP_154033_20160910_20200902_02_T1
2018-09-24	Landsat-8	LC08_L1TP_154033_20180924_20200830_02_T1
2019-09-12	Sentinel-2	S2A_MSIL2A_20190912T061631_N0213_R034_T42SVJ_20190912T085407
2020-09-21	Sentinel-2	S2B_MSIL2A_20200921T061629_N0214_R034_T42SVJ_20200921T084740
2021-09-21	Sentinel-2	S2A_MSIL2A_20210921T061631_N0301_R034_T42SVJ_20210921T082905
2022-09-16	Sentinel-2	S2A_MSIL2A_20220916T061641_N0400_R034_T42SVJ_20220916T101758
2023-09-13	Sentinel-2	S2B_MSIL2A_20230913T060639_N0509_R134_T42SVJ_20230913T092209
2024-09-15*	Sentinel-2	S2A_MSIL2A_20240915T061631_N0511_R034_T42SVJ_20240915T103349

*Glacier area extent also estimated.

Figure 4 displays the ice front withdrawal of GGP, based on the Moon and Joughin (2008) methodology, with the retreat being on the order of 200 m over for this 50-year period. In terms of surface area, GGP was estimated to be 0.55 km^2 in 1973 (Vladimirova et al., 1976), while in 2024 it was 0.41 km^2. This areal decrease of ~25% over this period is visualized in Fig. S2. The yearly appearance of GGP in the month of September during the 2018 to 2024 expeditions years displays the annual variation in snow conditions (Fig. S3). From this imagery it is especially visible how the snow conditions have diminished at an exceptional rate during the last years (2021–2024).

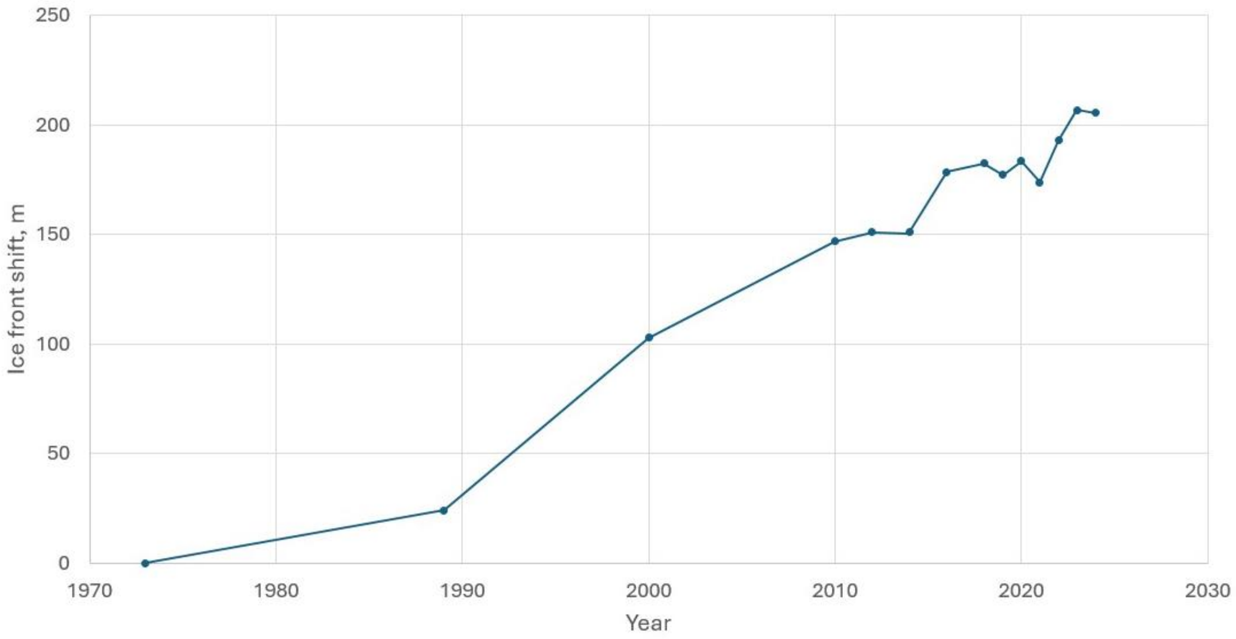

Figure 4. Shift of GGP terminus position from 1973 (Vladimirova et al., 1976) to 2024.

3.2 Aerial photography of GGP

During the expedition in 2018, 1478 images were collected with the DJI Phantom 4 Pro V2 drone. After Pix4D software initial setup 1323 images were successfully calibrated and 147 disabled, mostly due to not enough automatic tie points found on images because of nonoptimal camera orientation. The project assembly had seven natural ground check points (GCPs), and four natural check points (CPs). The average ground sampling distance (GSD) was 4.25 cm, and the imagery covered an area of 0.925 km^2. Similarly, in 2019, 615 images were collected with the DJI Phantom 4 Pro drone, and after Pix4D software initial setup 490 images were calibrated and 150 disabled, mostly due to not enough automatic tie points found on images because of nonoptimal camera orientation. The project assembly had five natural GCPs, three natural CPs, and 11 MTPs. The average GSD was 3.87 cm and the imagery covered an area of 0.767 km^2. In 2023, 515 images were collected with the DJI Phantom 4 Pro drone, and after Pix4D software initial setup 502 images were calibrated and 13 disabled, mostly due to not enough automatic tie points found on images because of nonoptimal camera orientation. The project assembly had two natural GCP, one CP – only one out of four recorded red cross marks on stakes' position were found on images, and three MTPs. The average GSD was 3.69 cm and the imagery covered an area of 0.286 km^2. During 2024, 407 images were collected with the DJI Phantom 4 Pro drone. After Pix4D software initial setup all images were successfully calibrated. During the expedition the position of 25 stakes were recorded, but unfortunately only seven out of 25 red cross marks on stakes' position were found on images. The project assembly had five GCP and two CP. The average GSD was 4.02 cm, and the imagery covered an area of 0.334 km^2. The resulting photogrammetric root-mean-square error of the different campaign years are listed in Table 4. In addition, the technical parameters of the photogrammetric workflow, including camera calibration, bundle block adjustment residuals, and GCP accuracy, are detailed for each year in the quality reports provided in the UAV aerial photography data sets. The DSM and orthomosaics (Fig. 5) indicate on high-resolution the glacier surface characteristics for each respective expedition years, and the dynamics occurring on year-to-year scale. 240

Table 4. Summary of localization accuracy per CP and mean errors in the three coordinate directions and average projection error in pixels.

Year	Number of GCPs	Number of CPs	Error X [m]	Error Y [m]	Error Z [m]	Average projection error [pixel]
2018	7	4	1.52	2.63	5.86	2.42
2019	5	3	1.71	0.99	4.52	0.63
2023	2	1	-0.07	-6.15	-22.91	0.85
2024	5	2	0.73	1.42	0.81	0.52

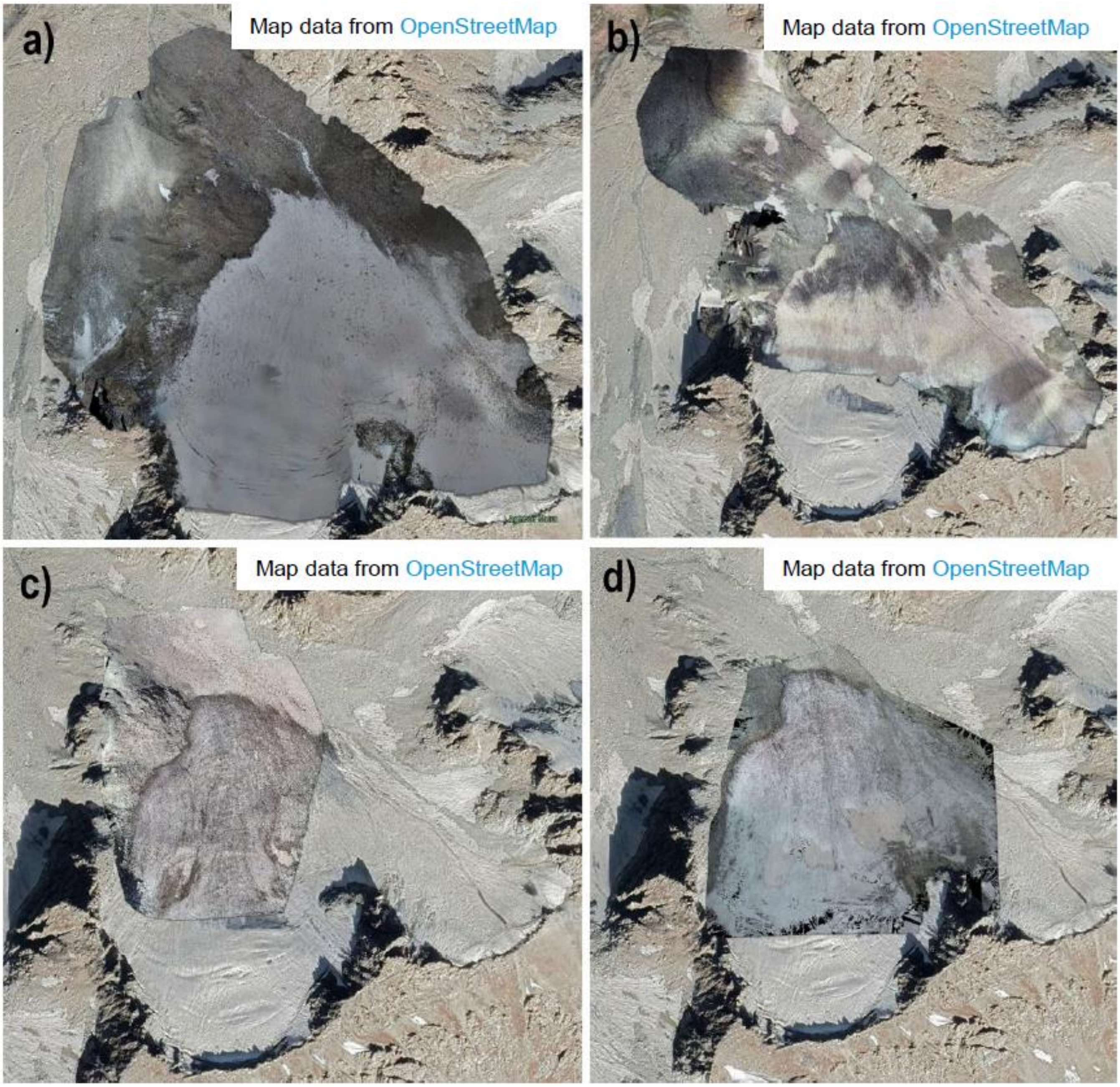

245 **Figure 5. Orthomosaic overlays of GGP generated by Pix4D software for each year: a) 2018, b) 2019, c) 2023 and d) 2024. Background image source OpenStreetMaps.**

3.3 GPS survey of GGP terminus

The glacier terminus position data from the GPS surveys consists of about 30 to 60 location data points and is available for the years 2018, 2023, 2024, and 2025. The collected data points are visualized in Fig. 6.

250 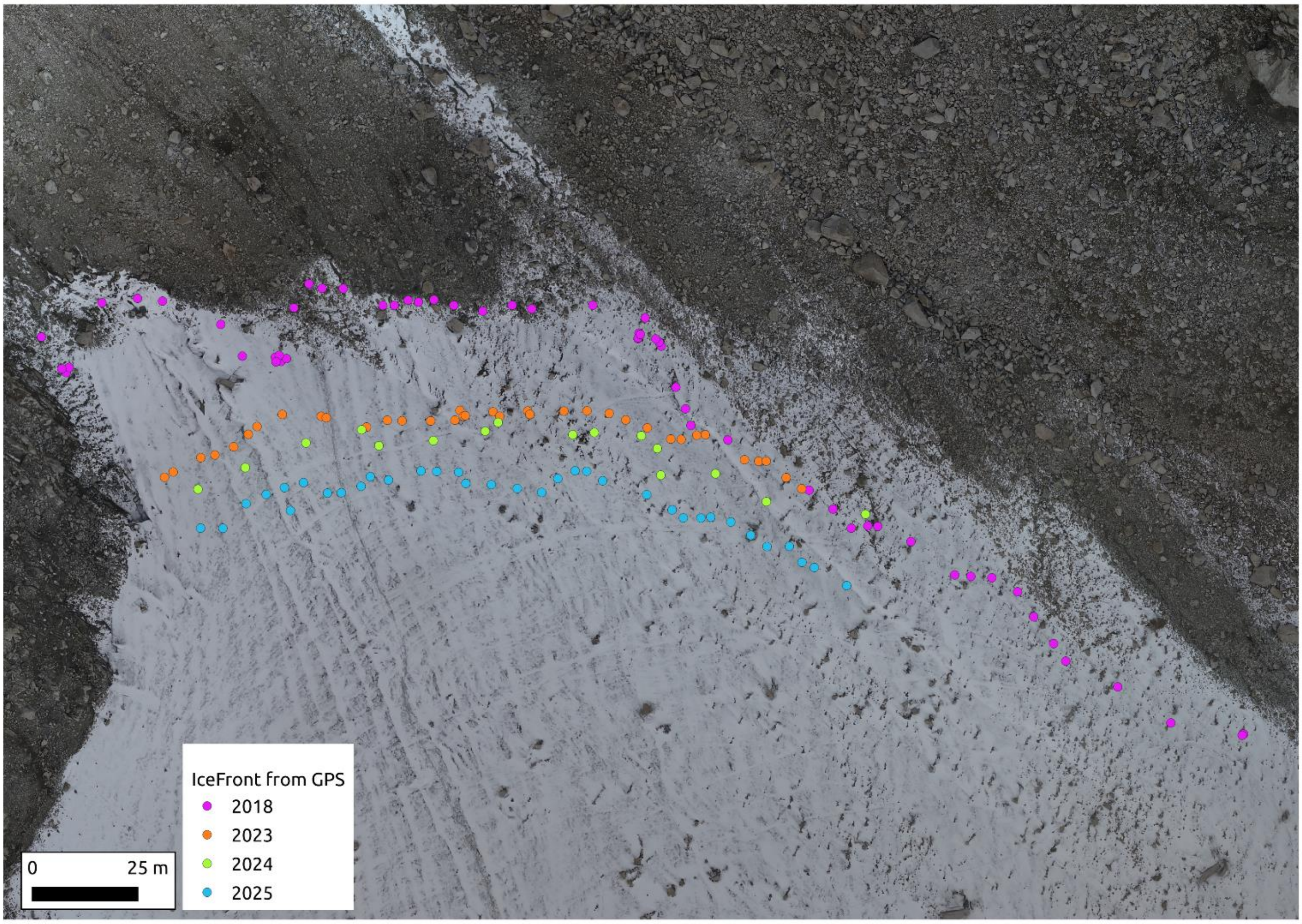

Figure 6. Ice front locations collected with GPS-surveys from different expedition years. Background image is from orthomosaic in 2018.

3.4 Time-lapse photography of GGP

The automatic camera images from 38.96491N, 68.26330E, 3275 m asl, encompass one year of observations (2023 expedition 255 to following year's field campaign). In 2024 the maximum snow extent was observed to occur at the end of March (Fig. 7a), while the minimum snow conditions took place in the middle of August (Fig. 7b), when snow was visually observed only at the upper sections of GGP. At the same time, from the images it is visible that more snow had ablated in 2023 compared to 2024, as shown in the yearly comparison pictures (Figs. 7c–d) taken in the beginning of September of 2023 and 2024.

https://doi.org/10.5194/essd-2025-609
Preprint. Discussion started: 3 March 2026

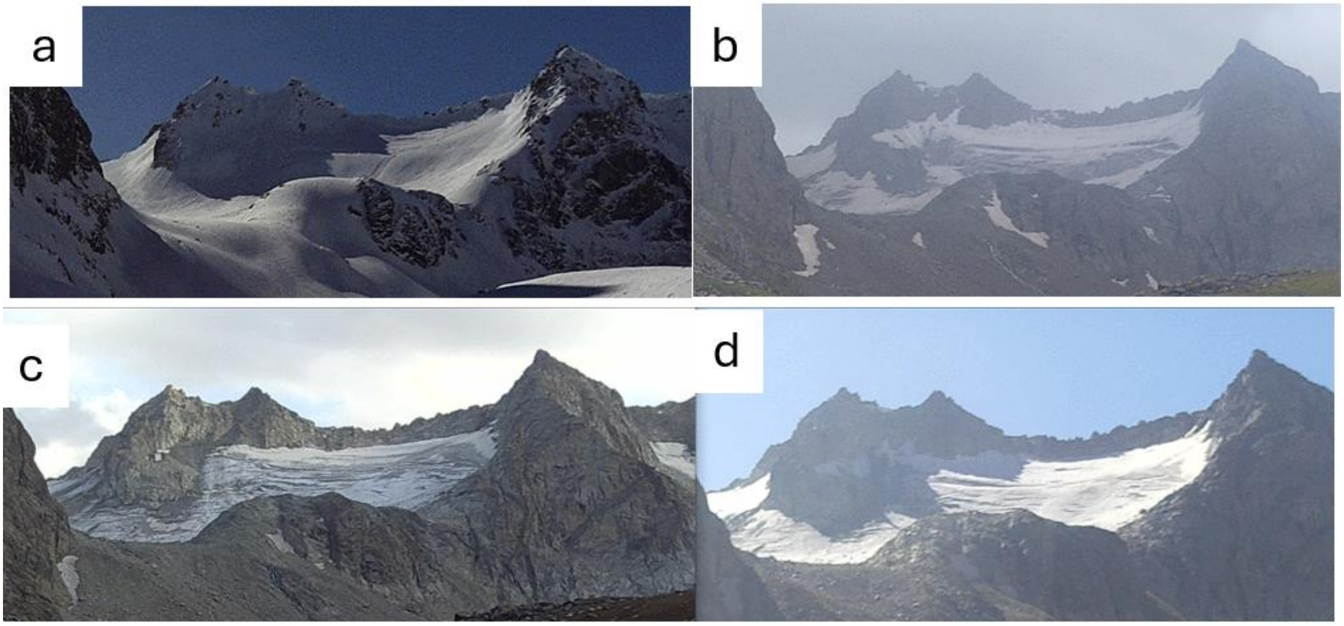

Figure 7. Snow conditions at GGP on a) 31.3.2024 (maximum snow conditions), b) 18.8.2024 (minimum snow conditions), c) 4.9.2023, and d) 4.9.2024.

3.5 Ablation stake survey

The first set of ablation stakes were installed in 2023, and the subsequent number of stake height recordings ranges from nine to 13, depending on if the stake was found the following year or not. In some instances, some stakes were completely melted out and found at a different location than the original installation place. These are marked accordingly in the data set file. The movement of the stakes from the 2023 to 2024 expedition, was laterally from -4 m to 11.5 m, with the longest movement in the steep section at the mid-section of GGP (at around 3680 m a.s.l). Near the bottom of the glacier, the movement was within the uncertainty of the GPS receiver, showing that there is very little lateral flow by glacier, rather only vertical melting.

3.6 Meteorological measurements

Meteorological measurements with the AWS are autonomous, with the data reported here at 10 min average values in the data repository (unless otherwise indicated).. The data points flagged as invalid by the sensors themselves were omitted from the data set. The AWS data contain two main gaps. The first took place during the first winter (starting 2018.12.31), when high snow accumulation covered the solar panel (and some of the sensors) and no power was available for the AWS. The measurements resumed automatically as the snow had melted on 2019.06.19. The second major data gap took place between 2021.09.13 (starting only a few days after completion of the 2021 expedition) and the 2023 expedition, when the main power switch to the AWS was found to be turned to the OFF-position due to an unknown reason. Measurements were resumed on 2023.9.19. An additional data gap is present in the wind sensor data (*WS* and *WD*) during periods 2019.9.13–2019.11.06 and

https://doi.org/10.5194/essd-2025-609
Preprint. Discussion started: 3 March 2026

2020.10.08–2021.09.31 due to bad data quality (data gaps and noisy measurements). The *SD* data during the period 2019.06.26–2019.09.03 were omitted due to an unknown technical issue that caused unrealistic values. The reported *T*, *p*, *RH*, *GI*, *WS*, and *WD* data are 1 h averages in Fig. 8. The reported *P* does not consider any wind undercatch corrections and is the cumulative precipitation for each hour and the reported *SD* and maximum *WS* are the maximum values for each hour. As a result of the high snow accumulation during the first winter at this location, the position of the AWS was changed in September of 2019 to a place with a lower expected snow buildup. Thus, the meteorological data is from two different locations (see Fig. 1b.). The first location was about 500 m from the glacier terminus (38.95541N, 68.27000E, 3390 m asl); while the second location is about 2 km from the glacier terminus (38.96491N, 68.26330E, 3275 m asl).

The time series of all the AWS measurement parameters are presented in Figs. 8. The discontinuity in *SD*, *p*, *WS*, and *WD* in September 2019 is due to moving the AWS to the new location. Monthly averages of the meteorological parameters are reported in Table 5 separately for the first and second location. The monthly averages were calculated only if there were more than 14 days of valid data. AWS measurements at the second location provided sufficient data for observation of seasonal variations. The monthly mean *T* varied from -9 to 11 °C, with the lowest mean values recorded in January and highest in July. The minimum and maximum mean daily *T* were -19 and 20 °C. *SD* varied greatly, but on average it peaked during March. A subtle seasonal variation was observed for *p*, varying from to 682 to 689 hPa with minimum in February and maximum in September. No clear seasonal variation has been observed for *RH*, *WS*, nor *WD*, being 55 %, 10 m s^{-1}, and 120°, respectively, on average. The maximum hourly mean of *WS* was 27 m s^{-1}, the maximum *P* was 57 mm d^{-1}, and the highest *SD* was 46 cm.

At the first location, AWS data exists only for July–August and October–December, whereas for the second location at a lower altitude, there are data for longer periods and extending over all the months. When the station was moved to the new location, the altitude of the AWS decreased about 115 m. Due to the lower altitude, there the average *p* in the new location was about 12 hPa higher. Lowering the altitude of the measurements causes also an increase in *T*, which was observed in a shift of about 2 °C. However, also surrounding landforms and surfaces (e.g., longer lasting snow cover) can affect the *T*. A probable reason for increased precipitation (about 0.3 mm d^{-1}) is that the precipitation gauge typically only detects liquid precipitation, which is more probable to occur more often at lower altitude with increased temperatures. On the opposite, the *SD* was considerably lower (about 53 cm between October–December) at the new location. Similarly, the prevailing wind moved from south-south-east to east-south-east in the new location, and the *WS* was about 3.5 m s^{-1} higher, which is probably due to the surrounding topography since the AWS was moved onto some elevated relief. The higher *WS* most likely also affects the *SD* as at higher *WS* snow drift redistributes snow effectively. Although this comparison was conducted only from five months of valid measurements in the first location, it still highlights the spatial variation of AWS parameters in the GGP basin.

https://doi.org/10.5194/essd-2025-609
Preprint. Discussion started: 3 March 2026

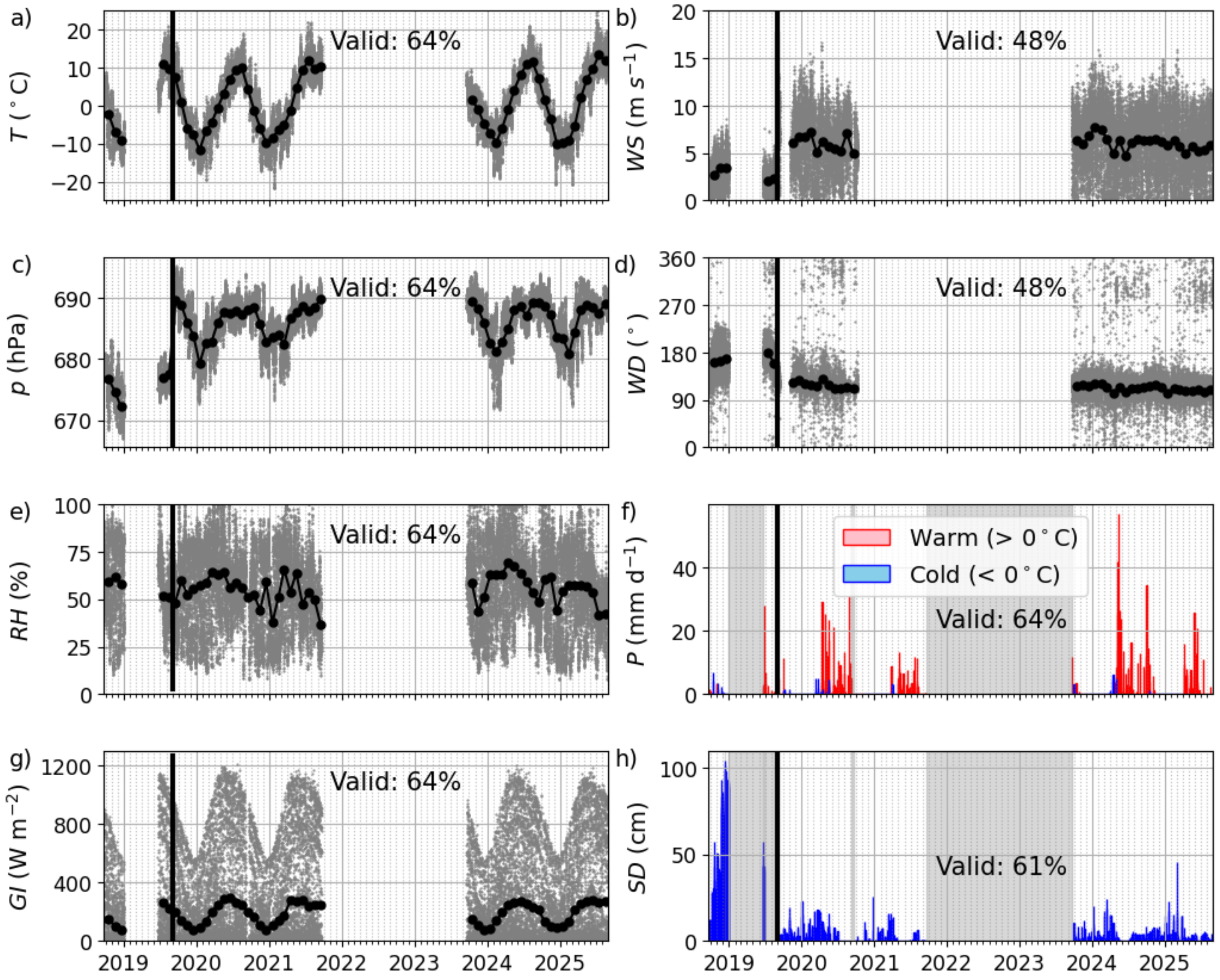

Figure 8. The time series of a) temperature (*T*), b) wind speed (*WS*), c) pressure (p), d) wind direction (*WD*), e) relative humidity (*RH*), f) daily precipitation (P), g) global irradiance (*GI*), h)) snow depth (*SD*) measured at GGP. The grey dots are the hourly data and the black line is the monthly mean (required 14 days of data). The black vertical line marks the day when the AWS was moved to another location. The precipitation is classified either as "warm" or "cold" depending if the mean temperature of the day was over of below 0 °C. The *P* is reported as the cumulative precipitation for each day and the *SD* is the maximum measured that day.

Table 5. Monthly means for each parameter measured by the AWS in the second location. The monthly averages in the first location are marked with an asterix (*). The averages are calculated from hourly data, but for *P* the averages were calculated from cumulated daily precipitation and *SD* from the daily maximum values. At least 14 days of valid data were required to derive averages.

month	*T* [°C]	*RH* [%]	*p* [hPa]	*GI* [W m^{-2}]	*P* [mm d^{-1}]	*WS* [m s^{-1}]	*WS*max [m s^{-1}]	*WD* [°]	*SD* [cm]
1	-9.3	52.9	682.2	95.6	0.0	6.7	11.3	116.2	2.8

2	-8.0	57.6	682.1	135.2	0.0	7.0	12.1	118.8	2.9
3	-5.3	62.6	683.1	195.0	0.2	5.7	9.9	118.5	5.0
4	-0.3	60.9	686.4	256.1	1.3	5.4	9.3	122.6	2.4
5	4.7	62.9	688.0	272.5	4.0	5.9	10.0	120.6	0.9
6	8.5	55.2	688.2	281.6	1.3	5.1	8.7	118.8	0.4
7	11.4 10.9*	53.3 51.6*	687.6 676.9*	257.3 266.1*	1.1 0.3*	5.5 2.0*	9.5 4.9*	126.6 182.2*	1.3
8	10.7 9.7*	50.5 51.1*	688.4 677.5*	246.4 221.1*	0.9 0.1*	6.5 2.3*	10.5 6.2*	117.1 163.8*	1.0
9	6.9	48.6	689.4	211.4	1.0	6.2	10.4	120.7	1.4
10	0.7 -2.3*	57.8 59.0*	688.9 676.7*	145.5 148.6*	0.6 0.6*	6.2 2.7*	10.6 6.8*	120.2 161.3*	2.0 25.0*
11	-4.1 -6.9*	50.6 61.9*	686.7 647.7*	104.0 101.5*	0.1 0.3*	6.1 3.4*	10.3 8.2*	120.4 165.2*	2.0 52.8*
12	-8.0 -9.2*	52.3 57.9*	684.0 672.3*	80.4 74.8*	0.0 0.0*	6.5 3.4*	10.9 8.2*	119.4 167.4*	1.5 86.4*

3.7 Glacier snow chemistry

The snow impurity data set consists of 21 samples collected in 2018 and 29 samples collected in 2019. During the other expedition years most of the glacier snow had been ablated, and no snow samples could be collected. In general, the August–September campaigns were not an optimal time of the year for snow sampling, but this period for the field work was dictated, for instance, by measurements of the seasonal end of glacier ablation and accessibility to GGP. In 2018, one snow pit (38.94393N 68.27794E, 3812 m a.s.l) was dug to a depth of 100 cm, from which snow samples were collected. The filtered samples were analyzed for carbonaceous particle content. In 2019, two snow pits were excavated, with the first one located in the higher section of the glacier (essentially same place as the 2018 snow pit), while the second snow pit was in a lower section (38.94695N, 68.27727E, 3666 m a.s.l) of the glacier. The first 2019 snow pit was 280 cm deep, from which ten samples were collected at different intervals slabs. From this snow pit (referred to as pit 1 in 2019 data), both trace elements and carbonaceous particles were analyzed. The second snow pit of 2019 was 210 cm deep (referred to as pit 2 in 2019 data), and from this pit ten snow samples were collected throughout the pit and analyzed for trace elements and carbonaceous particles. For some of the reported snow pit samples (both 2018 and 2019) the filter substrates ended up becoming too particle loaded while filtering to obtain reliable carbonaceous quantification with the used analytical procedure. These samples are marked with NaN in the snow chemistry data files.

The surface snow samples (n = 9, referred to as 2019 surface samples) were collected in two locations of GGP in 2019 a few meters away from the pits where visually different appearing particulates were present on the glacier surface (which were part of the reflectance measurements). These surface samples were analyzed for ionic compounds concentrations. In proximity to pit 1, snow samples were collected from snow surfaces appearing black-pink, brownish, and black-grey (with the corresponding sample IDs of 13, 11, 7, respectively). For the surface snow samples collected in the vicinity of pit 2, the different sampling spots are illustrated in Fig. 9. The corresponding sampling IDs are 21–22, 23–24, 25–26 for the brown, black, and red-pink spots, respectively.

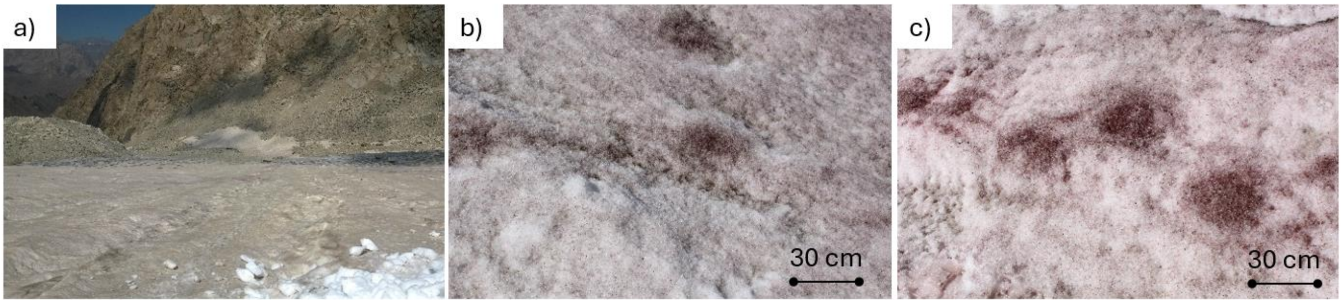

Figure 9. Surface snow characteristics observed in 2019 expedition that were sampled and measured: typical brownish deposits looking down from the mid-glacier a), blackish deposits b) and red-pink deposits c).

The highest snow impurity content was measured in the surface of pit 1 in 2019, with elevated carbonaceous particles and trace elements, which were dominated by aluminum and iron at 18.1 µg ml^{-1} and 12.0 µg ml^{-1}, respectively. A secondary elevated impurity layer was observed at the bottom of the pit, and this layer can possibly be interpreted as the previous year's surface layer with the higher concentration being due to melt amplification (Doherty et al., 2013). Between these layers, the impurity concentrations remained relatively low, about 10% of those in the surface layer. A similar pattern for snow impurities was observed in pit 2.

3.8 Glacier surface reflectance

Before snow surface sampling in 2019, reflectance measurements were taken at spots representative of the sampled areas. In the upper section of the glacier (next to pit 1), three different surface types were measured, while in the midsection of GGP, three additional measurements focused on impurity-rich areas commonly found across the snow surface (which are visualized in Fig. 9). During the 2023 campaign, the snow on the glacier surface was mostly ablated. Eighteen reflectance measurements were carried out laterally across the glacier within the 3600–3680 m a.s.l. elevation range. The reflectance curves shown here are based on nadir observations; therefore, angular dependence should be considered when comparing these data to remote sensing measurements taken at off-nadir angles. Examples of measured reflectance are presented in Figs. 10a–c. In 2019, the highest values were recorded in the upper section, ranging from about 0.70 at wavelengths below 400 nm to 0.95 near 700 nm. The midsection showed similar spectral shapes but lower values (0.25–0.55). Both zones were associated with visually brownish impurities which had similar chemical compound signatures. The black and red impurity spots in the midsection had even lower reflectance (Fig. 10b), which had coinciding chemical compositions, with elevated ammonium amounts. For the 2023 reflectance measurements, the curves were consistently low, remaining close to 0.20 across all wavelengths (Fig. 10c).

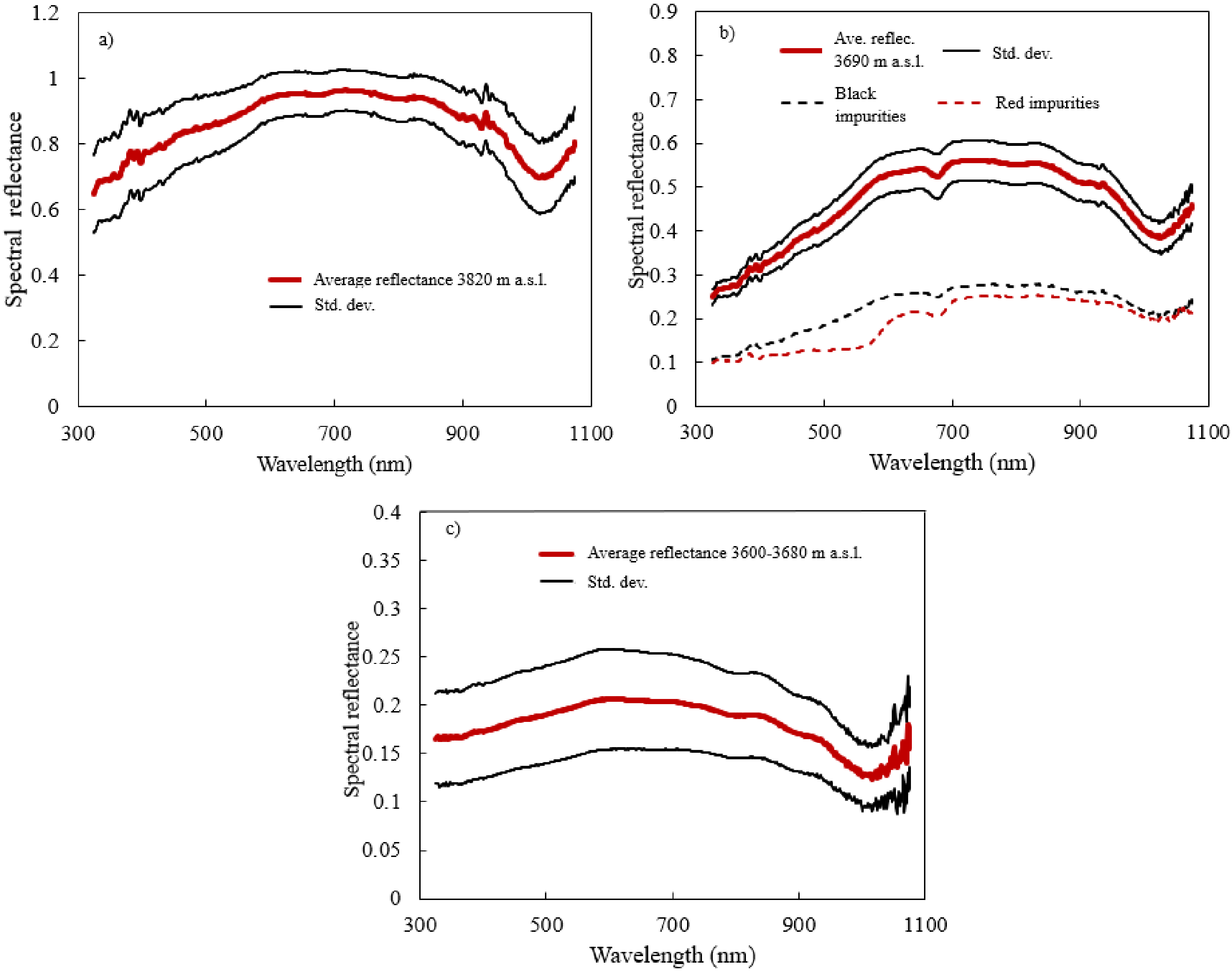

Figure 10. Average reflectance and standard deviation of reflectance measurements of the glacier surface with black, brownish and red impurities. a) Higher section of GGP 2019. b) Mid-section of GGP in 2019. c) Ablation zone in 2023.

3.9 Atmospheric aerosol

Atmospheric aerosols were measured during all expeditions, except in 2024 and 2025. The most extensive data set is available of the aerosol absorption, from which black carbon can be derived based on the absorption at wavelength 880 nm. In 2021 and 2023, absorption was additionally measured at four other wavelengths: 625, 528, 470 and 375 nm. The aerosol parameters also include total particle number concentrations and optical particle size distribution (reported as PM_1, $PM_{2.5}$ and PM_{10} mass concentrations assuming unit density), which were sporadically measured during the 2018 expedition (yielding 5.5 h of data in total).

The aerosol data was measured at either one min or five min time resolution and processed to one-hour average values. In the reported data, we compare data only measured at the expedition base camp or while at the GGP glacier. Aerosol instruments were primarily operated during daytime hours due to issues of weather sensitivity and battery lifetime. However, in 2023, a continuous measurement of black carbon concentrations was conducted over a period of 43 hours to obtain an indication of diurnal variability at the site.

Black carbon concentrations ranged from 200 ng m^{-3} (25th percentile) up to 930 ng m^{-3} (75th percentile) during individual expeditions with average campaign concentrations varying between 400 ng m^{-3} and 550 ng m^{-3} (Fig. 11). These values are relatively high for a remote location, similar to those encountered in European background locations (e.g, Savadkoohi et al., 2023). The average absorption Ångström exponent derived from the wavelength dependence of the absorption coefficient was 1.45 during the 2023 campaign, indicating based on the "Aethalometer model" (Sandradevi et al., 2008) that 58% of the absorption was caused by fossil fuel burning sources, and 42% by biomass burning sources.

Particle number- and particulate mass concentrations were measured only for a brief period in 2018. Therefore, the values may not be representative of the prevailing atmospheric conditions. However, as these are the very first data of its kind from the region, they are discussed here. The observed particle number concentration was 1850 ± 810 cm^{-3}, which is similar to levels measured in European rural areas (Rose et al., 2021), while the PM_1, $PM_{2.5}$ and PM_{10} concentrations were 5.6 ± 0.3 µg m^{-3}, 7.5 ± 1.1 µg m^{-3} and 14.6 ± 6.4 µg m^{-3}, respectively. The $PM_{2.5}$ concentration was 50% of the WHO's 24-hour guideline value of 15 µg m^{-3} and 32% of the 24-hour PM_{10} guideline value of 45 µg m^{-3}.

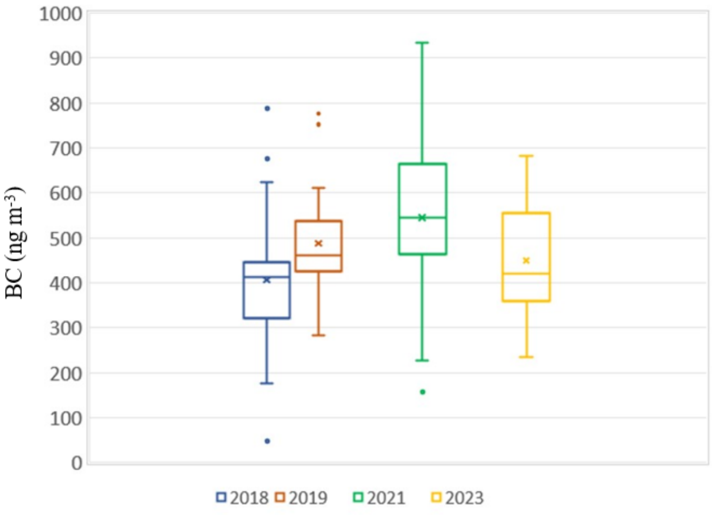

Figure 11. Black carbon (BC) concentration distributions during expedition periods in 2018–2023, with the boxes representing 25th and 75th percentiles and the line and cross inside the box are the median and mean, respectively. The outer lines represent the 10th and 90th percentiles

4. Summary and conclusions

This paper present cryospheric and atmospheric data sets that have been collected from the Zarafshon River Basin and GGP glacier in Tajikistan (Svensson et al., 2026). Starting in 2018, with the installation of an AWS during the first field campaign, data has been collected in annual field expeditions until 2025 (except in 2020 and 2022). The in situ glaciological observations have been made over different spatial resolutions, and include terminus location, ablation stakes, snow conditions, as well as characterizing the glacier with UAV aerial photography. Complimentary satellite imagery, with a different temporal resolution dating back to 1989, was processed for this work to further compare and characterize GGP. The surface conditions of the glacier were determined during field campaigns with synchronized surface reflectance measurements and snow sample chemical analysis. In addition, atmospheric aerosols were characterized at selected times. Meteorological parameters from the AWS have been continuously measured since the installation in 2018 and have over 60% data coverage until 2025. The data presented here consists of a diverse set of parameters, that can be used as input variables to, or validation of models, as well as ground truthing for remote sensing. More specifically, the overall glacier changes over long time periods or the high precision orthomosaics offer the possibility to study both fine and coarse scale processes occurring at the glacier. The combination of ground-based spectral reflectance and concurrent snow chemistry data for glacier surfaces are rare, yet most valuable for verifying model results or remote sensing observations on glacier surface. This is especially true coupled to the darkening of the glacier surface, by snow impurities. The spectral data presented for this particular natural environment is invaluable since they are measured for different snow impurities. Combined with the snow chemistry data set, the surface radiative budget of the glacier can be further studied.

With recent reports of unprecedent loss of glaciers and snow mass in different environments globally (e.g., Hassan et al., 2024; Menounos et al., 2025), it is of great interest for the community to have access to in situ observational data, especially in regions where data are scarce.

5. Data availability

The data sets are freely available at the public FMI data repository METIS, https://doi.org/10.57707/fmi-b2share.t4vwg-gf542 (Svensson et al., 2026), last accessed: February 5, 2026. Satellite imagery used in this manuscript can be freely acquired in google earth engine. The data report from 1973 expedition is available upon request from the Tajikhydromet (Vladimirova et al., 1976).

Author contributions

The preparation and execution of field expeditions were made by JSv., RR, AH, MS, TJ, AH, DR, HK, DB, VL, KL, AL, GPF, EA, and AH. Data processing was conducted or assisted by JSv, RR, KN, AH, MS, DB, VL, KL, AL, GPF, MR, OM, JSt, EA, AH. The paper was written by JSv and AH with input from co-authors. All authors have agreed on the submitted version of this manuscript.

Competing interests

The authors declare that they have no conflict of interest.

Acknowledgements

The authors wish to thank the support and hard work by numerous people throughout the different expeditions. JSv acknowledges the support from the Otto Malm foundation.

Financial support

This work has been supported by the ministry of foreign affairs of Finland through the projects FINTAJ II and III. This work has also been supported by the Atmosphere and Climate Competence Center (ACCC) of the Research Council of Finland (projects 337552, 357904, 359342), and by the Black and Brown Carbon in the Atmosphere and the Cryosphere (BBrCAC project no. 341271).

References

Aizen, V., Aizen, E., and Melack, J.: Climate, snow cover, glaciers, and runoff in the Tien Shan, Central Asia, Water Resour., 31, 1113–1129, 1995.

Barandun, M., Fiddes, J., Scherler, M., Mathys, T., Saks, T., Petrakov, D., and Hoelzle, M.: The state and future of the cryosphere in Central Asia, Water Secur., 11, 100072, doi.org/10.1016/j.wasec.2020.100072, 2020.

Barandun, M. and Pohl, E.: Central Asia's spatiotemporal glacier response ambiguity due to data inconsistencies and regional simplifications, Cryosphere, 17, 1343–1371, doi.org/10.5194/tc-17-1343-2023, 2023.

Beck, H.E., Wood, E.F., McVicar, T.R., Zambrano-Bigiarini, M., Alvarez- Garreton, C., Baez-Villanueva O.M., McVicar, T.R., Sheffield, J. and Karger, D.N.: Bias Correction of Global High-Resolution Precipitation Climatologies Using Streamflow Observations from 9372 Catchments. J. Climate, 33, 1299–1315, doi.org/10.1175/JCLI-D-19-0332.1, 2020.

Birch, M. E. and Cary, R. A.: Elemental carbon-based method for monitoring occupational exposures, to particulate diesel exhaust, Aerosol Sci. Tech., 25, 221–241, doi.org/10.1080/02786829608965393, 1996.

Cavalli, F., Viana, M., Yttri, K. E., Genberg, J., Putaud, J.-P.: Toward a standardised thermal-optical protocol for measuring atmospheric organic and elemental carbon: the EUSAAR protocol, Atmos. Meas. Tech., 3, 79–89, doi.org/10.5194/amt-3-79-2010, 2010.

Chen, Y., Li, W., Deng, H., Fang, G., and Li, Z.: Changes in Central Asia's Water Tower: Past, Present and Future, Sci.,Rep., 6, 35458, https://doi.org/10.1038/srep35458, 2016.

Cogley, J. G., Hock, R., Rasmussen, L. A., Arendt, A.A., Bauder, A., Braithwaite, R. J., Jansson, P., Kaser, G., Möller, M., Nicholson, L., and Zemp, M.: Glossary of Glacier Mass Balance and Related Terms, IHP-VII Technical Documents in Hydrology No. 86, IACS Contribution No. 2, UNESCO-IHP, Paris, doi.org/10.5167/uzh-53475, 2011.

Doherty, S. J., Grenfell, T. C., Forsstrom, S., Hegg, D. L., Brandt, R. E., and Warren, S. G.: Observed vertical redistribution of black carbon and other insoluble light-absorbing particles in melting snow, J. Geophys. Res.-Atmos., 118, 5553–5569, doi.org/10.1002/jgrd.50235, 2013.

Hassan W.U., Nayak M.A., Saharwardi, M.S., Dar, J.A., Dasari, H.P., Hoteit, I., Abualnaja, Y.: Unveiling the devastating effect of the spring 2022 mega-heatwave on the South Asian snowpack. Commun Earth Environ., 5, doi.org/10.1038/s43247-024-01857-y, 2024.

Hoelzle, M., Azisov, E., Barandun, M., Huss, M., Farinotti, D., Gafurov, A., Hagg, W., Kenzhebaev, R., Kronenberg, M., Machguth, H., Merkushkin, A., Moldobekov, B., Petrov, M., Saks, T., Salzmann, N., Schöne, T., Tarasov, Y., Usubaliev, R., Vorogushyn, S., Yakovlev, A., and Zemp, M.: Re-establishing glacier monitoring in Kyrgyzstan and Uzbekistan, Central Asia, Geosci. Instrum. Method. Data Syst., 6, 397–418, https://doi.org/10.5194/gi-6-397-2017, 2017.

Marks, D. and Dozier, J.: Climate and energy exchange at the snow surface in the alpine region of the Sierra Nevada 2. Snow cover energy balance. Water Resour. Res. 28, 3043–3054, doi.org/10.1029/92WR01483, 1992.

Menounos, B., Huss, M., Marshall, S., Ednie, M., Florentine, C., and Hartl, L.: Glaciers in Western Canada-conterminous US and Switzerland experience unprecedented mass loss over the last four years (2021–2024). Geophys. Res. Lett., doi.org/10.1029/2025GL115235, 2025.

Moon, T., and I. Joughin, I.: Changes in ice front position on Greenland's outlet glaciers from 1992 to 2007, J. Geophys. Res., 113, F02022, doi:10.1029/2007JF00092, 2008.

Pohl, E., Gloaguen, R., Andermann, C., and Knoche, M.: Glacier melt buffers river runoff in the Pamir Mountains, Water Resour. Res., 53, 2467–2489, 2017.

Pritchard, H.D.: Asia's shrinking glaciers protect large populations from drought stress, Nature, 569, 649–654, doi.org/10.1038/s41586-019-1240- 1, 2019.

Pritchard, H. D.: Global data gaps in our knowledge of the terrestrial cryosphere, Front. Clim., 3, 689823, doi.org/10.3389/fclim.2021.689823, 2021.

Rose, C., Collaud Coen, M., Andrews, E., Lin, Y., Bossert, I., Lund Myhre, C., Tuch, T., Wiedensohler, A., Fiebig, M., Aalto, P., Alastuey, A., Alonso-Blanco, E., Andrade, M., Artíñano, B., Arsov, T., Baltensperger, U., Bastian, S., Bath, O., Beukes, J. P., Brem, B. T., Bukowiecki, N., Casquero-Vera, J. A., Conil, S., Eleftheriadis, K., Favez, O., Flentje, H., Gini, M. I., Gómez-Moreno, F. J., Gysel-Beer, M., Hallar, A. G., Kalapov, I., Kalivitis, N., Kasper-Giebl, A., Keywood, M., Kim, J. E., Kim, S.-W., Kristensson, A., Kulmala, M., Lihavainen, H., Lin, N.-H., Lyamani, H., Marinoni, A., Martins Dos Santos, S., Mayol-Bracero, O. L., Meinhardt, F., Merkel, M., Metzger, J.-M., Mihalopoulos, N., Ondracek, J., Pandolfi, M., Pérez, N., Petäjä, T., Petit, J.-E., Picard, D., Pichon, J.-M., Pont, V., Putaud, J.-P., Reisen, F., Sellegri, K., Sharma, S., Schauer, G., Sheridan, P., Sherman, J. P., Schwerin, A., Sohmer, R., Sorribas, M., Sun, J., Tulet, P., Vakkari, V., van Zyl, P. G., Velarde, F., Villani, P., Vratolis, S., Wagner, Z., Wang, S.-H., Weinhold, K., Weller, R., Yela, M., Zdimal, V., and Laj, P.: Seasonality of the particle number concentration and size distribution: a global analysis retrieved from the network of Global Atmosphere Watch (GAW) near-surface observatories, Atmos. Chem. Phys., 21, 17185–17223, doi.org/10.5194/acp-21-17185-2021, 2021.

Sandradewi, J., Prévôt, A., Szidat, S., Perron, N., Alfarra, M., Lanz, V., Weingartner, E., and Baltensperger, U.: Using aerosol light absorption measurements for the quantitative determination of wood burning and traffic emission contributions to particulate matter, Environ. Sci. Technol., 42, 3316–3323, doi:10.1021/es702253m, 2008.

Savadkoohi, M., Pandolfi, M., Reche, C., Niemi, J. V., Mooibroek, D., Titos, G., Green, D. C., Tremper, A. H., Hueglin, C., Liakakou, E., Mihalopoulos, N., Stavroulas, I., Artiñano, B., Coz, E., Alados-Arboledas, L., Beddows, D., Riffault, V., De Brito, J. F., Bastian, S., Baudic, A., Colombi, C., Costabile, F., Chazeau, B., Marchand, N., Gómez-Amo, J. L., Estellés, V., Matos, V., van der Gaag, E., Gille, G., Luoma, K., Manninen, H. E., Norman, M., Silvergren, S., Petit, J.-E., Putaud, J.-P., Rattigan, O. V., Timonen, H., Tuch, T., Merkel, M., Weinhold, K., Vratolis, S., Vasilescu, J., Favez, O., Harrison, R. M., Laj, P., Wiedensohler, A., Hopke, P. K., Petäjä, T., Alastuey, A., and Querol, X.: The variability of mass concentrations and source apportionment analysis of equivalent black carbon across urban Europe, Environ. Int., 178, 108081, doi.org/10.1016/j.envint.2023.108081, 2023.

Svensson, J., Rakhmonov, R., Nazirzoda, K., Shodmonov, M., Brus, D., Le, V., Luoma, K., Lemos, A., Ruppel, M., Meinander, O., Ström, J., Asmi, E., Fogwill, G. P., Hojiev, A., Jurabekov, T., Hiyoev, A., Rahimzoda, D., Kholzoda, H., & Hyvärinen, A.-P.: Data for manuscript:"Atmospheric and cryospheric observations at the high-altitude Zarafshon River Basin and the hydrographic party glacier (GGP), Tajikistan" [Data set]. Finnish Meteorological Institute. https://doi.org/10.57707/fmi-b2share.t4vwg-gf542, 2026.

Svensson, J., Ström, J., Kivekäs, N., Dkhar, N. B., Tayal, S., Sharma, V. P., Jutila, A., Backman, J., Virkkula, A., Ruppel, M., Hyvärinen, A., Kontu, A., Hannula, H.-R., Leppäranta, M., Hooda, R. K., Korhola, A., Asmi, E., and Lihavainen, H.: Light-absorption of dust and elemental carbon in snow in the Indian Himalayas and the Finnish Arctic, Atmos. Meas. Tech., 11, 1403–1416, doi.org/10.5194/amt-11-1403-2018, 2018.

Vladimirova, V.N., Uskov, Y.S., Kuznetsov, N.A., Department of Hydrometeorology of the Tajik SSR Technical report on glaciological work on the GGP ice cap, Main Department of Hydrometeorological Service of the USSR CM, Dushanbe 1976.

World Health Organization, WHO global air quality guidelines: particulate matter (PM2.5 and PM10), ozone, nitrogen dioxide, sulfur dioxide and carbon monoxide, (2021), ISBN: 9789240034228.

You, Q., Cai, Z., Pepin, N., Chen, D., Ahrens, B., Jiang, Z., Wu, F., Kang, S., Zhang, R., Wu, T., Wang, P., Li, M., Zuo, Z., Gao, Y., Zhai, P., and Zhang, Y.: Warming amplification over the Arctic Pole and Third Pole: Trends, mechanisms and consequences, Earth Sci. Rev., 217, 103625, doi.org/10.1016/j.earscirev.2021.103625, 2021.

Zhang, Y., Kang, S., Gao, T., Kang, S., Shangguan, D., and Luo, X.: Albedo reduction as an important driver for glacier melting in Tibetan Plateau and its surrounding areas, Earth Sci. Rev., 220, 103735, https://doi.org/10.1016/j.earscirev.2021.103735, 2021.

Zech, C., Schöne, T., Illigner, J., Stolarczuk, N., Queißer, T., Köppl, M., Thoss, H., Zubovich, A., Sharshebaev, A., Zakhidov, K., Toshpulatov, K., Tillayev, Y., Olimov, S., Paiman, Z., Unger-Shayesteh, K., Gafurov, A., and Moldobekov, B.: Hydrometeorological data from a Remotely Operated Multi-Parameter Station network in Central Asia, Earth Syst. Sci. Data, 13, 1289–1306, doi.org/10.5194/essd-13-1289-2021, 2021.